

Extracellular vesicles released by cancer-associated fibroblast-induced myeloid-derived suppressor cells inhibit T-cell function

Carlo P. Ramil¹, Handan Xiang², Peng Zhang^{3*}, Aileen Cronin^{4#}, Lisia Cabral⁵, Zhizhang Yin⁶, Josephine Hai^{7†}, Huijun Wang^{8‡}, Benjamin Ruprecht^{9**}, Yanlin Jia^{10##}, Dongyu Sun^{11††}, Hongmin Chen^{12‡‡}, and An Chi¹³

¹Chemical Biology, Merck & Co. Inc, Cambridge, MA, USA; ²Discovery Immunology, Merck & Co. Inc, Cambridge, MA, USA; ³Neuroimmunology, Merck & Co. Inc, Boston, MA, USA; ⁴Quantitative Biosciences, Merck & Co. Inc, Boston, MA, USA; ⁵Computational and Structural Chemistry, Merck & Co. Inc, Kenilworth, NJ, USA

ABSTRACT

Myeloid cells are known to play a crucial role in creating a tumor-promoting and immune suppressive microenvironment. Our previous study demonstrated that primary human monocytes can be polarized into immunosuppressive myeloid-derived suppressor cells (MDSCs) by cancer-associated fibroblasts (CAFs) in a 3D co-culture system. However, the molecular mechanisms underlying the immunosuppressive function of MDSCs, especially CAF-induced MDSCs, remain poorly understood. Using mass spectrometry-based proteomics, we compared cell surface protein changes among monocytes, *in vitro* differentiated CAF-induced MDSCs, M1/M2 macrophages, and dendritic cells, and identified an extracellular vesicle (EV)-mediated secretory phenotype of MDSCs. Functional assays using an MDSC/T-cell co-culture system revealed that blocking EV generation in CAF-induced MDSCs reversed their ability to suppress T-cell proliferation, while EVs isolated from CAF-induced MDSCs directly inhibited T-cell function. Furthermore, we identified fructose biphosphatase 1 (FBP1) as a cargo protein that is highly enriched in EVs isolated from CAF-induced MDSCs, and pharmacological inhibition of FBP1 partially reversed the suppressive phenotype of MDSCs. Our findings provide valuable insights into the cell surface proteome of different monocyte-derived myeloid subsets and uncover a novel mechanism underlying the interplay between CAFs and myeloid cells in shaping a tumor-permissive microenvironment.

ARTICLE HISTORY

Received 16 May 2023
Revised 5 December 2023
Accepted 27 December 2023

KEYWORDS

Cancer-associated fibroblasts (CAF); extracellular vesicles (EV); myeloid-derived suppressor cells (MDSC); proteomics

Introduction

Immune checkpoint therapies, including PD1/PD-L1 inhibitors, have revolutionized cancer treatment by enhancing anti-tumor immunity. However, resistance to these therapies remains a significant challenge in achieving durable clinical responses.¹ Myeloid cells, which are highly abundant in the tumor microenvironment (TME), may contribute to resistance to PD1/PD-L1 inhibitors via different mechanisms and play a crucial role in promoting an immunosuppressive TME.² Myeloid-derived suppressor cells (MDSCs) and M2 macrophages are examples of myeloid subsets that can suppress T-cell activation. These cells express inhibitory receptors such as ILT3 or ligands such as VISTA, which directly engage immune checkpoint receptors expressed on T-cells to curb T-cell activation.³ Additionally, myeloid cells can secrete immuno-modulatory cytokines, such as IL-10, and extracellular vesicles to induce immunosuppressive responses.⁴ Thus, a comprehensive understanding of the cell surface proteomes

of myeloid cell subsets will shed light on molecular mechanisms underlying immunosuppression and provide novel combinatorial strategies.

Mass spectrometry-based proteomics has emerged as a valuable tool for identifying protein determinants that mediate immunosuppressive effects.⁵ The proteomes of murine myeloid cells, especially MDSCs, have been extensively studied and well characterized.⁶ Previous studies have focused on the total proteomes of myeloid cell subsets and identified altered expression of membrane receptors, endocytosis, and intracellular vesicle trafficking of MDSCs.⁶ However, these studies did not include primary human myeloid cells, and whether the findings from these studies translate into the human system remains unknown.

In our previous study, we uncovered the important role of cancer-associated fibroblasts (CAFs) in educating tumor-infiltrating monocytes and polarizing them into MDSCs under a 3D culture condition.⁷ We profiled and compared

CONTACT Carlo P. Ramil  carlo.ramil@merck.com; An Chi  an_chi@merck.com  Chemical Biology, Merck & Co., Inc, 320 Bent St, Cambridge, MA 02141

*Present address: Eurofins PSS Insourcing Solutions, Cambridge MA USA.

#Present address: Takeda Pharmaceuticals, Cambridge MA USA.

†Present address: Bristol Myers Squibb, Cambridge MA USA.


‡Present address: Deerfield Management Company, L.P. New York NY USA.

**Present address: Covant Therapeutics, Boston MA USA.

##Present address: Keythera Pharmaceuticals, Jiangsu, PRC.

††Present address: Flagship Pioneering Lab 94, Cambridge MA USA.

‡‡Present address: WARF Therapeutics, Madison WI USA.

 Supplemental data for this article can be accessed online at <https://doi.org/10.1080/2162402X.2023.2300882>.

© 2024 Merck & Co., Inc., Rahway, NJ, USA and its affiliates. Published with license by Taylor & Francis Group, LLC.

This is an Open Access article distributed under the terms of the Creative Commons Attribution-NonCommercial License (<http://creativecommons.org/licenses/by-nc/4.0/>), which permits unrestricted non-commercial use, distribution, and reproduction in any medium, provided the original work is properly cited. The terms on which this article has been published allow the posting of the Accepted Manuscript in a repository by the author(s) or with their consent.

the proteomes of dendritic cells and CAF-induced MDSCs (CAF-MDSCs) and identified increased expression of NOX2 in MDSCs.⁷ NOX2 produces reactive oxygen species that directly hinder CD8⁺ T-cell proliferation. However, our understanding of the myeloid cell subtypes derived from human primary monocytes at protein levels remains incomplete, preventing the identification of key molecular mechanisms underlying immunosuppression in the TME.

In this study, we aimed to gain a deeper understanding of the cell surface proteome changes in human primary monocyte-derived myeloid cell subsets, which are essential for intercellular communication and can regulate T-cell functions. To achieve this, we explored multiple proteomics methods to capture cell surface proteins and selected an SP3-based method⁸ to quantify the cell surface protein changes among myeloid cell subsets, with a particular focus on CAF-MDSCs. We captured some of the reported immuno-modulatory cell surface molecules, such as ILT3 (LILRB4) and PD-L1 (CD274). By relating observed proteomic changes to biological processes, we identified pathways enriched in vesicle-mediated transport and increased extracellular vesicle (EV) production in MDSCs. We subsequently performed functional assays to demonstrate that MDSC-derived EVs contribute to the immunosuppressive effect on T-cells. Our findings provide a valuable resource for cell surface proteomics of myeloid subsets and inform the development of immunotherapy strategies to reverse immunosuppression triggered by MDSCs and CAFs in the TME.

Materials and methods

Ethics statement

All primary human lung squamous cell carcinoma (LSCC) samples used in this study were obtained from the Clinical and Translational Science Institute (CTSI) at the University of Minnesota, with patient consent approved by the Institutional Review Board protocol #0305M47681 in accordance with ethical standard of the US Common Rule and the Belmont Report. The CTSI is supported through the NIH, grant UL1TR002494. Human peripheral whole blood was purchased from STEMCELL Technologies, Inc. with donor's informed consent.

Primary human cells

Primary human CD4 T-cells from healthy donors were purchased from Biological Specialty Company (#215-07-10). Tumor infiltrating lymphocytes (TIL) were expanded from fresh tumor in the presence of IL-2 for 2 weeks. CD19⁺, CD8⁺, and CD4⁺ cells were isolated sequentially from 6 million cells of TIL by magnetic activated cell sorting using CD19 Microbeads (Miltenyi Biotec #130-050-301), CD8 Microbeads (Miltenyi Biotec #130-045-201), and CD4 Microbeads (Miltenyi Biotec #130-045-101), respectively. Regulatory T-cells were isolated from 6 million cells of TIL using EasySep Human CD4⁺CD127^{low}CD25⁺ Regulatory T Cell Isolation Kit (STEMCELL Technologies, #18063). Human squamous cell carcinoma fibroblasts CAF1 were purchased from Vitro Biopharma (#CAF07-S); CAF2 and CAF3 were derived from freshly resected tumor samples purchased from

the University of Minnesota, and patient clinicopathologic features were described previously.⁷ Cells were allowed to expand in complete growth medium: RPMI1640 + Glutamax (Gibco #61870036), 10% heat deactivated FBS (Sigma-Aldrich #F4135), 10 mM HEPES (Gibco #15630080), 1 mM sodium pyruvate (Gibco #11360070), 1X non-essential amino acid (Gibco #11140050), and 10 U/mL Penicillin-Streptomycin (Gibco #15140122). CD14⁺ monocytes were isolated from peripheral blood mononuclear cells (PBMC) using CD14 microbeads (Miltenyi Biotec #130-050-201) following manufacturer's instructions. PBMC were isolated from fresh human peripheral blood leukopak (STEMCELL Technologies #70500.1) using Lymphoprep (STEMCELL Technologies #07851) and Sepmate (STEMCELL Technologies #85450).

Sample preparation for total protein measurements

One million CD4 T-cells, or between 0.8 and 2 million cells for each TIL sub-type, were lysed in 50 μ L sodium deoxycholate (SDC) lysis buffer. The SDC lysis buffer consists of 1% SDC (Sigma-Aldrich #30968), 10 mM TCEP (Tris(2-carboxyethyl) phosphine hydrochloride, Sigma-Aldrich #75259), 40 mM CAA (2-chloroacetamide, Sigma-Aldrich #22790) in 50 mM TEAB. Samples were incubated at 95°C for 15 minutes then cooled down to room temperature. Reduced and alkylated proteins were digested using Trypsin/Lys-C (Promega #V5072) overnight at 37°C. Digested peptides were purified using the Phoenix kit (PreOmics # P.O.00023). One million CD14⁺ monocytes and differentiated cells – cancer-associated fibroblast-induced myeloid-derived suppressor cells (CAF-MDSC), immature dendritic cells (iDC), M1 macrophages (M1), and M2 macrophages (M2) were lysed in either SDC lysis buffer or SP3 lysis buffer. SP3 lysis buffer is composed of 5% SDS, 10 mM TCEP, 55 mM CAA, in 50 mM TEAB (Triethylammonium bicarbonate, Thermo #90114). Peptide clean-up was performed following a published protocol.⁸

Sample preparation for cell surface protein measurements

Cell surface labeling were performed using Pierce cell surface protein isolation kit (Thermo #89881) using the sulfo-NHS-SS-biotin reagent. Additional reagents used for labeling are NHS-biotin (Thermo, #20217) or alkoxyamine-biotin (Thermo, #26137) or alkoxyamine-SS-biotin (Thermo, #26138). Briefly, ten million CD4 T-cells (Biospecialty #215-07-10) were resuspended in ice-cold DPBS (Gibco #14190144) then treated with cell surface labeling reagents following manufacturer's recommendation. Labeled cells were processed following the iST protocol⁹ using a 5% SDC lysis buffer consisting of 5% sodium deoxycholate (Sigma-Aldrich #30968), 10 mM TCEP (Tris(2-carboxyethyl) phosphine hydrochloride, Sigma-Aldrich #75259), 40 mM CAA (2-chloroacetamide, Sigma-Aldrich #22790) in 50 mM Tris, pH 8.5. Samples were incubated at 95°C for 15 minutes then cooled down to room temperature. Reduced and alkylated proteins were digested using Trypsin/Lys-C (Promega #V5072) in 50 mM TEAB overnight at 37°C. Digested peptides were purified using the Phoenix kit (PreOmics # P. O.00023).

Sample preparation for EV protein measurements

Purified EVs (25 µg) were resuspended in SP3 lysis buffer and processed as described above. Tandem Mass Tag (TMT) plexes were separated by donor. Each TMT10-plex contains duplicate samples of EVs from four cell types from one donor and one pooled sample, leaving the last channel empty. TMT-labeled peptides were fractionated using high pH reversed phase fractionation on an Agilent 1100 HPLC system equipped with a XBridge Peptide BEH C18 column (130 Å, 3.5 µm, 2.1 mm x 150 mm; Waters) at a constant flow rate of 0.25 mL/min. A 200-µg solution of peptides solvent A (20 mM NH₄HCO₂, 10% ACN, pH 10) was separated by increasing solvent B (20 mM NH₄HCO₂, 90% ACN, pH 10) to a concentration of 10% in 5 min, to 35% in 55 min, 55% in 5 min and to 100% in 5 min. Next, 100% B was held constant for 5 min before switching back to 0% B in 1 min, and column re-equilibration at 0% B for 14 min. A total of 72 fractions were collected in a 96-well plate in 1 min intervals from 0 min to 72 min (A01 to A12 followed by B12 to B01 and so on). Fractions were combined by pooling rows A, C, E and B, D, F for a total of 24 final fractions. Pooled peptide fractions were dried down and resuspended in 0.2% formic acid in water.

Liquid chromatography – tandem mass spectrometry (LC-MS/MS)

A 10 µL solution of peptides was loaded to an Acclaim™ PepMap™ 100 C18 trap column (100 µm I.D. x 2 cm length, 5 µm particle size, Thermo Scientific) at a flow rate of 10 µL/min in 100% solvent A (0.1% FA in HPLC grade water). After 5 min of loading and washing, peptides were transferred to an analytical column (whole proteome: EASY-Spray™, 75 µm I.D x 75 cm, 2 µm particle size; enriched samples and TMT-labeled samples: EASY-Spray™, 75 µm I.D x 50 cm, 2 µm particle size, Thermo Scientific) and separated at a flow rate of 300 nL/min using a 300 min (whole proteome) or 120 min (enriched samples and TMT-labeled samples) non-linear gradient from 5% to 38% solvent B (0.1% FA in HPLC grade ACN). Subsequently, the solvent B concentration was increased to 70% and held constant for 10 min followed by a decrease to 3% solvent B for 1 min and re-equilibration at 3% solvent B for 10 min. The overall method duration was 332 min and 152 min, respectively, from injection to injection. The mass spectrometer (whole proteome and enriched samples: Q Exactive HF, Thermo Fisher Scientific) was operated in data dependent mode, automatically switching between MS1 and MS2 spectra (MS/MS). MS1 spectra were acquired at a resolution of 120,000 in the Orbitrap using an automatic gain control (AGC) target value of 1e6 with a maximum injection time of 50 ms. Up to 20 peptide precursors were selected for fragmentation by higher energy collision-induced dissociation (HCD) with an isolation width of 1.2 Th, a maximum injection time of 40 ms, an AGC target value of 1e3, 27% normalized collision energy (NCE) and a resolution of 15,000. Dynamic exclusion was set to 30 s and singly

charged precursors were excluded. Whole proteome samples were injected twice. Fractionated TMT-labeled samples were analyzed in Orbitrap Fusion Lumos mass spectrometer (Thermo Fisher Scientific) where MS3 fragmentation was employed to reduce TMT-related ratio compression effects.¹⁰ MS1 spectra were acquired using the following parameters: a resolution of 120,000, an AGC target value of 1e6, and maximum injection time of 100 ms. The top 20 precursors were selected for MS2 scans with collision-induced dissociation (CID) fragmentation using the following parameters: resolution 35,000, AGC 1e6, maximum injection time 100 ms, isolation window 0.7 Th, and normalized collision energy (NCE) 35%. Singly charged species were excluded from MS2 analysis and dynamic exclusion was set to automatic. MS3 quantification scans were performed using ten SPS ions with a resolution of 50,000, NCE of 55% and maximum injection time of 86 ms.

Mass spectrometry data processing and analysis

Peptide and protein identification and quantification were performed using MaxQuant¹¹ version 1.6.14 for label-free samples and version 1.6.17 for TMT samples. MS2 data were searched against the Swissprot reference database (human proteins 42,233 entries; downloaded 16.08.2017) using the embedded search engine Andromeda. Carbamidomethylated cysteine was set as fixed modification; Oxidation of methionine, and N-terminal protein acetylation were set as variable modifications. Trypsin/P was specified as the proteolytic enzyme with up to two missed cleavage sites allowed. Fragment ion tolerance was set to 20 ppm. For label-free samples, the ‘match-between-runs option’ (0.5 min match time window) was enabled. Search results were filtered for a minimum peptide length of 7 seven amino acids, 1% peptide and protein false discovery rate. Default settings were kept for all other parameters.

Further processing and analysis were done using the Perseus software v1.6.14.0¹² Reverse hits, proteins marked with “only identified by site” and potential contaminants were removed. Intensity values were log2 transformed and normalized to the median intensity. For label-free analysis, 50% of valid values in total were allowed. Missing values were randomly imputed from a normal distribution. For each condition the median of the log2 protein intensity distribution was shifted 1.8 standard deviations to lower values and the width was set to 0.3 standard deviations compared to the original distribution of measured values. For TMT analysis, cross-plex normalization was done by median centering for each protein within each plex (row-wise normalization).¹³ Differential abundance analysis was performed using two-sample student’s t-test with Benjamini-Hochberg false discovery rate correction. Venn diagram analyses were done using the web tool Venny 2.1 (Venny, RRID: SCR_016561) (<https://bioinfogp.cnb.csic.es/tools/venny/>). Pathway and process enrichment analyses were done in Metascape (<https://metascape.org/>).¹⁴ Gene ontology enrichment and protein network analyses were done in STRING (<https://string-db.org/>).¹⁵

CAF-MDSC generation

CAF-MDSC were generated as described previously.⁷ Briefly, monocytes were isolated from PBMC using CD14 MicroBeads (Miltenyi Biotec # 130-050-201). To generate CAF-MDSC, 2 million monocytes were added to the bottom well of a 6-well plate containing 2 mL complete media with 20 ng/mL GM-CSF (R&D Systems #215-GM) containing 1 million cells of 3D CAF culture in a transwell insert. Media was replaced at day 4 and cells were collected at day 7 then used in subsequent assays.

iDC generation

Isolated monocytes were cultured in ImmunoCult™ DC Differentiation Medium (STEMCELL Technologies #10987 and #10988) following manufacturer's instructions. Briefly, 2 million monocytes per well were seeded in a 6-well plate (Corning #3471) containing 2 mL of media. Cells were differentiated for 7 days, and media was replaced on day 4. Cells were collected on day 7 and used in subsequent assays.

M1 and M2 macrophage generation

Isolated CD14+ monocytes (2 million per well) were cultured in 2 mL ImmunoCult™ -SF Macrophage Medium (STEMCELL Technologies #10961) supplemented with 50 ng/mL M-CSF (STEMCELL #78057) for 4 days. On day 4, (1) for M1 activation, media was supplemented with 10 ng/mL LPS and 50 ng/mL IFN γ (#78020); (2) for M2a activation, media was supplemented with 10 ng/mL IL-4 STEMCELL (#78045). Cells were collected on day 7 and used in subsequent assays.

T-cell suppression assay

Autologous CD8+ T-cells were isolated from PBMC using EasySep™ Human CD8+ T-Cell Isolation Kit (STEMCELL Technologies # 17953). Isolated cells were labeled with CFSE (Invitrogen # C34554) and resuspended in complete media at 1 million cells/mL. On day 7 of MDSC generation, differentiated cells were detached using Detachin (Genlantis #T100100) and resuspended in complete media at 1 million cells/mL. CFSE-labeled CD8+ T-cell (T) and MDSC (M) were combined at a ratio of 2:1 (100,000:50,000) T:M in a 96-well plate (Corning #7007) containing IL-2 (Gibco # PHC0026), CD3/CD28 beads (Thermo #11161D) and filled with complete media to a final volume of 200 μ L. Nonproliferating control does not contain CD3/CD28 beads and T-cell only control does not contain MDSC. For compound treatments, cells were treated at EC90 concentration of the inhibitors used: 300 nM of nSMase2i (EC50 = 30 nM) or the inactive control; 300 nM of CA2i (EC50 = 1 nM), 100 nM of MMP9i (EC50 = 10 nM), and 10 μ M of FBPI1 (EC50 = 1 μ M). Vehicle control used is DMSO (2 μ L). For EV treatment, isolated EVs from a 3-day culture were purified and added to T-cells. After 3 days, cells were collected for FACS analysis. Cells were washed with FACS buffer (2% FBS, 1 mM EDTA in DPBS) and stained with Live/Dead NIR dye (Biolegend #423106) for 30 mins then with PE anti-human CD8 antibody (Clone SK1, Biolegend #344706,

RRID:AB_1953244) for 30 mins. Cells were fixed using BD Cytofix and FACS analysis was performed in BD LSRFortessa or BD FACSymphony A3 flow cytometer (BD Biosciences). Data analysis was performed in FlowJo v. 10.6.2 or v. 10.9.0 (FlowJo). The percentage of suppression was calculated using the established formula: $((\text{Log}_2(y)$ of T-cell alone – $\text{Log}_2(y)$ of T-cell+Myeloid cells)/ $\text{Log}_2(y)$ of T-cell alone) x 100, where y is the mean fluorescence intensity (MFI) of CFSE on the whole population divided by the MFI of CFSE of non-proliferating cells.¹⁶

Extracellular vesicle (EV) isolation

Following the 7-day differentiation of CAF-MDSC, media was replaced with 2 mL complete media containing exosome-depleted FBS (Systembio #EXO-FBSHI-50A-1) and cultured for additional 3 days. Conditioned media was collected and EVs were isolated by size exclusion chromatography (SEC) for functional assays or by PureExo® exosome isolation kit (101Bio #P101L) for LC-MS/MS analysis. SEC was performed using qEV2 columns (Izon Science LTD) with the qEV Automated Fraction Collector (Izon Science LTD). Thirteen 2-mL fractions were collected per sample and concentrated to a final volume of 0.5 mL using Amicon® Ultra-15 Centrifugal Filter Unit (Millipore #UFC9010).

EV characterization

EV size, count, and purity were characterized using nanoparticle tracking analysis.¹⁷ Each sample was diluted accordingly and loaded onto Nanosight NS300 (Malvern Panalytical) using a 1-mL disposable syringe. Five captures were recorded per measurement of samples. Data were analyzed using NanoSight NTA software v3.40 (Malvern Panalytical). Surface marker expression on EVs were measured by flow cytometry analysis as described.¹⁸ Briefly, EVs were captured on Streptavidin magnetic beads (Millipore # LSKMAGT10) coated with biotinylated anti-human CD9 (Biolegend #312112) and anti-human CD81 (Biolegend #349514) antibodies then stained with PE-conjugated anti-human CD63 (Biolegend #353004) or anti-human CD81 (Biolegend #349506) or anti-human CD9 (Biolegend #312106) or mouse IgG1 κ isotype antibody (Biolegend #400114).

Statistical analysis

Statistical analysis was performed using GraphPad Prism 9 (GraphPad). Statistical tests applied are indicated in the figure legends. Differences were considered statistically significant when $p \leq 0.05$.

Data availability

All processed and normalized data shown in the manuscript are available as Supplementary Tables 1 and 2. The mass spectrometry proteomics data have been deposited to the ProteomeXchange Consortium via the PRIDE¹⁹ partner repository with the dataset identifiers PXD035259 and PXD035248.

Results

Changes in the cell surface proteome during CAF-induced monocyte-to-MDSC differentiation

To maximize the coverage of membrane proteins, we tested several methods for enrichment of cell surface proteins using detergents and commercially available kits and reagents based on chemical labeling of surface amines and glycans (Supplementary Fig. S1). Performance of each method was assessed based on the number of identified proteins containing one or more predicted transmembrane domain (TMD) according to MDM²⁰ housed in the Human Protein Atlas (<https://www.proteinatlas.org/>) (Supplementary Fig. S1a). The in-stage tip (iST) method gave the highest coverage of membrane proteins from primary human lymphocytes (Supplementary Fig. S1a – c). Next, we compared iST with the single-pot, solid-phase-enhanced sample preparation (SP3)⁸ workflow to assess cell surface proteome coverage in myeloid cells. We found a ~25% increase in the total protein

identification and ~20% increase in cell surface protein identification using SP3 compared to iST (Supplementary Fig. S1d). We selected the SP3 sample processing workflow in subsequent experiments due to the increased cell surface proteome depth.

We next sought to understand the proteomic differences of monocytes and monocyte-derived MDSCs by utilizing the MDSC-generating protocol we previously reported (Figure 1a).⁷ We compared the cell surface proteome of monocytes before and after co-culturing with CAFs. From a total of 5399 proteins quantified in both cell types, 1145 proteins are annotated as cell surface proteins (Supplementary Table S1 and Figure 1b). Comparative analysis using a two-sample t-test returned 526 and 160 cell surface proteins that are significantly up- or downregulated compared to the starting monocytes, respectively (FDR <0.05) (Figure 1b). Cell surface proteins identified in CAF-MDSC include CD14, CD33, ITGAM, and members of the S100 family (Supplementary Table 1). The differentially expressed

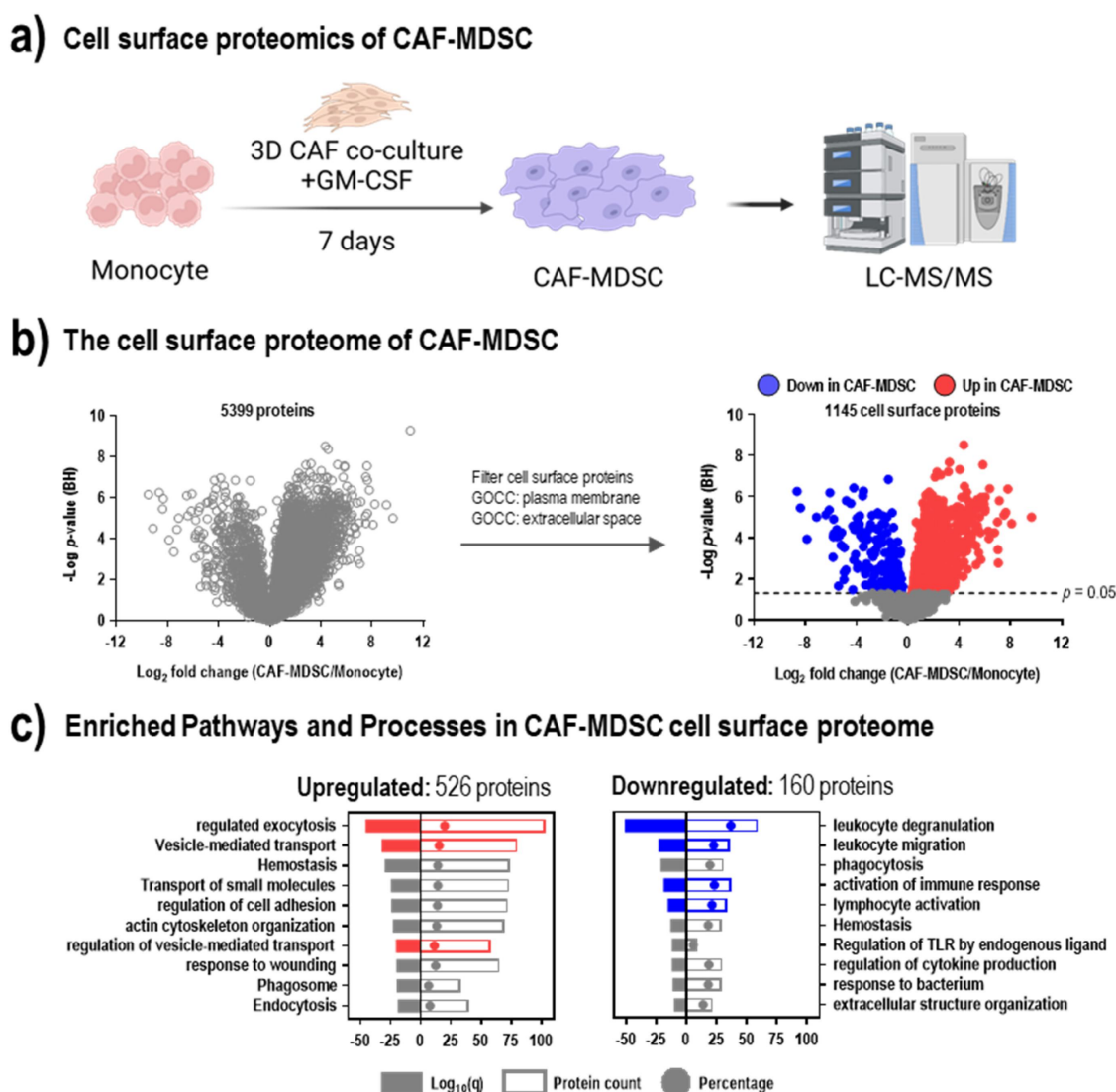


Figure 1. Changes in the cell surface proteome during monocyte-to-MDSC differentiation show the upregulation of vesicle-related pathways. (a) Monocytes were differentiated to CAF-MDSC and subjected to label-free proteomics. (b) Differential protein expression analysis of cell surface proteins in CAF-MDSCs vs. monocytes; cell surface proteins were filtered based on gene ontology cellular component (GOCC) terms ‘plasma membrane’ and ‘extracellular space’; colored dots represent significantly altered proteins (red = up; blue = down) (c) Enriched pathway and process terms based on differentially expressed proteins in CAF-MDSC using metaspase.

proteins were annotated and analyzed using Metascape¹⁴ (<http://metascape.org>) to identify altered pathways and processes (Figure 1c). Proteins downregulated in CAF-MDSCs were engaged in leukocyte degranulation (GO:0043299), migration (GO:0050900), and lymphocyte activation (GO:0046649) (highlighted in blue), which suggest previously described functions of MDSCs related to their interaction with other immune cells (Figure 1c). Significant terms enriched in the upregulated proteins in CAF-MDSCs include ‘regulated exocytosis’ (GO:0045055), ‘vesicle-mediated transport’ (R-HSA-5653656), and ‘regulation of vesicle-mediated transport’ (GO:0060627) (highlighted in red) (Figure 1c). These terms suggest an increase in the bulk transport of proteins and other (bio)molecules through vesicles.

The cell surface proteome of CAF-MDSC

To investigate if the vesicle-mediated secretory phenotype is specific to CAF-MDSCs, we generated diverse monocyte-derived subsets – immature dendritic cells (iDC), M1 macrophages (M1), and M2 macrophages (M2) to compare their cell surface proteomes by LC-MS/MS (Figure 2a). Principal component analysis of cell surface protein profiles shows differences that are driven by the cell types (Figure 2b). Cluster analysis of cell surface proteins (1195 proteins) identified in all myeloid cell subsets revealed a group of cell surface proteins enriched in CAF-MDSC (cluster #10) (Supplementary Fig. S2a). This cluster is comprised of 93 proteins that are highly expressed in CAF-MDSCs derived from 3 donors (Supplementary Fig. S2b). Metascape analysis of this cluster

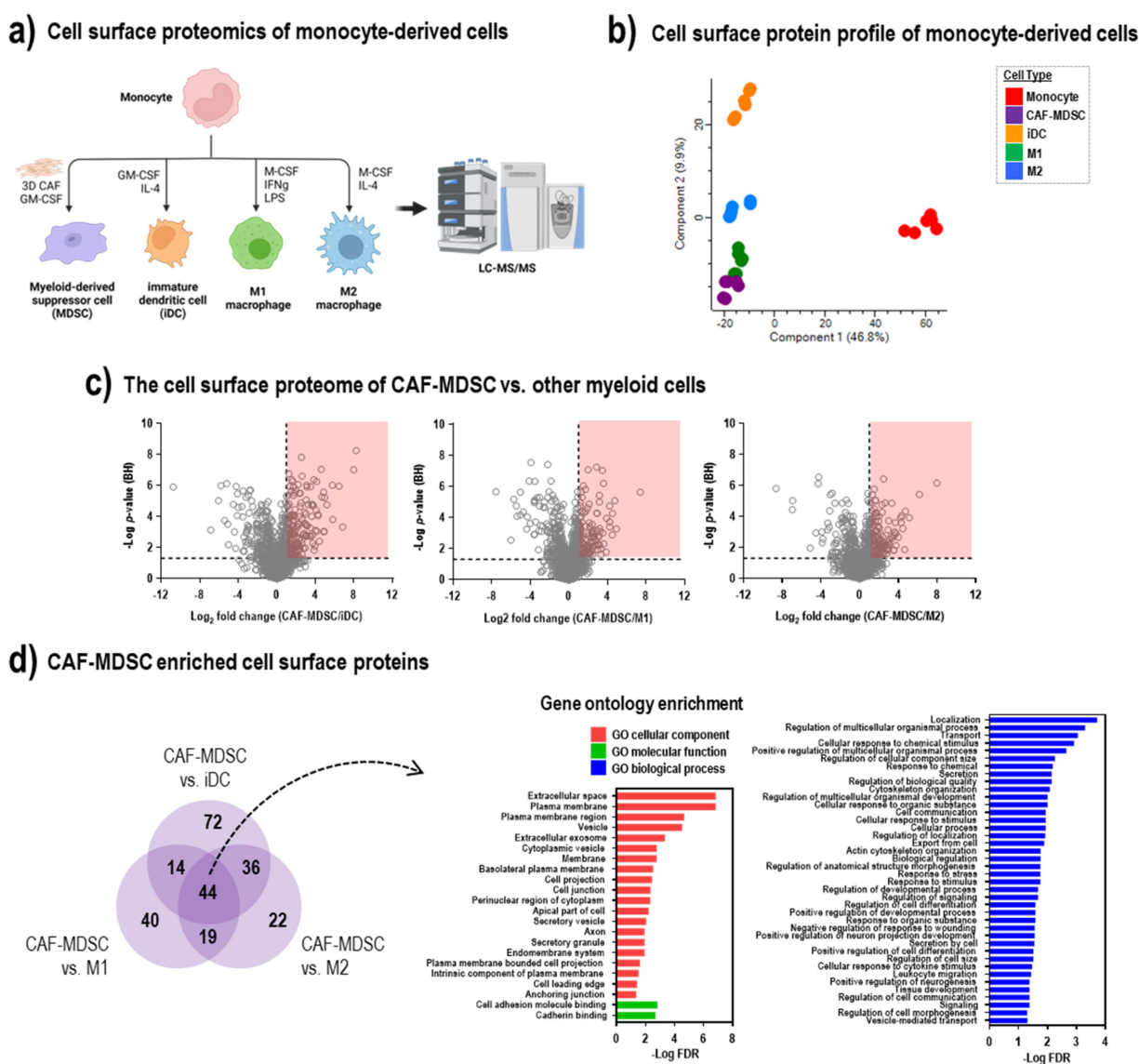


Figure 2. The cell surface proteome of CAF-MDSC is enriched in proteins. (a) Monocytes were differentiated to cancer-associated fibroblast-induced myeloid derived suppressor cells (CAF-MDSC), immature dendritic cells (iDC), M1 and M2 macrophage and subjected to label-free proteomics. (b) Principal component analysis of the cell surface proteome profile of monocytes and differentiated cells – CAF-MDSC, iDC, M1 and M2 macrophage. (c) Differential protein expression analysis of cell surface proteins in CAF-MDSC vs. iDC or M1 or M2 macrophage; cell surface proteins were filtered based on GOCC terms ‘plasma membrane’ and ‘extracellular space’; significantly enriched cell surface proteins in CAF-MDSC (fold change > 2; FDR < 0.05) are enclosed in red box (dotted line on x-axis; Log₂ = 1.0; y-axis: p-value (BH) = 0.05). (c) Overlap of significantly enriched cell surface proteins in CAF-MDSC vs. other cell types. (d) Gene ontology enrichment of significantly enriched cell surface proteins in CAF-MDSC (44 proteins) using STRING DB.

shows pathway enrichment in ‘vesicle-mediated transport’ (R-HSA-5653656) (Supplementary Fig. S2c, highlighted in red). Moreover, cluster #10 is also enriched in terms related to its known functions in supporting the extracellular matrix, cell migration, and immune cell activation (Supplementary Fig. S2c, highlighted in orange). Next, the total quantified proteins in each cell type (CAF-MDSC, iDC, M1, M2) were compared to the levels in the starting monocytes using student’s t-test (Supplementary Fig. S2d). Significantly enriched proteins that were annotated as cell surface proteins (fold change > 2; FDR < 0.05) were filtered and subjected to functional protein association networks analysis using the STRING¹⁵ database (Supplementary Fig. S2e). Out of the 468 cell surface proteins significantly enriched in CAF-MDSCs, 189 (40%) are annotated as ‘vesicle’ (GO:0031982). In iDCs, none of the 197 significantly enriched cell surface proteins are annotated as vesicle proteins. Both macrophage populations had similar proportion of vesicle proteins; 53 out of 145 proteins in M1 (37%) and 55 out of 148 proteins (37%) in M2, which were ~ 3.5-fold lower in number than CAF-MDSCs. To identify uniquely enriched proteins in CAF-MDSCs, we compared the cell surface proteome of CAF-MDSCs to the other populations – iDC, M1, and M2 using student’s t-test (Figure 2c). We found 44 cell surface proteins that were significantly enriched in CAF-MDSCs (Figure 2d). Gene ontology enrichment of these 44 proteins revealed that the most significant terms include ‘vesicle’, ‘extracellular exosome’, ‘secretory vesicle’, ‘secretion’, ‘export from cell’ and ‘vesicle-mediated transport’ (Figure 2e). Taken together, by comparing to monocytes or monocyte-derived myeloid cell subsets, our proteomic analysis revealed that CAF-MDSCs possess a unique secretory phenotype by producing extracellular vesicles, which can have an impact on the crosstalk between MDSCs and T-cells. This prompted us to further investigate if CAF-MDSC-derived EVs contribute to the immunosuppressive function of CAF-MDSCs.

Suppression of T-cell proliferation by CAF-MDSC EVs

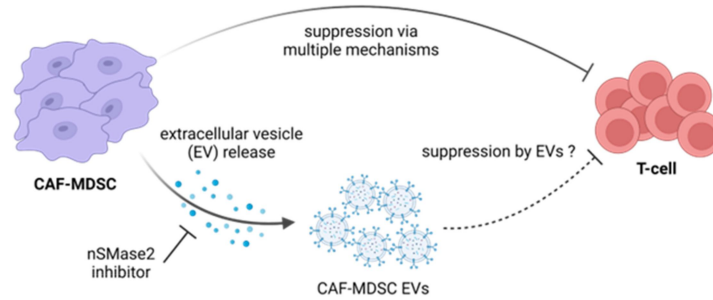
CAF-MDSCs potently suppress autologous T-cell proliferation through multiple mechanisms (Figure 3a).⁷ To investigate whether the release of EVs from CAF-MDSCs impacts immune suppression, we treated the co-culture of CAF-MDSCs and autologous CD8+ T-cells with an inhibitor of nSMase2 (neutral sphingomyelinase 2), a key enzyme in the biosynthesis of ceramide required for the generation of EVs (Fig. 43b).²¹ Treatment with the nSMase2 inhibitor (nSMase2i)²² significantly decreased the ability of CAF-MDSCs to suppress the proliferation of T-cells while treatment with the inactive form of the nSMase2i did not show any significant change in the proliferation of T-cells, showing that the reduction in T-cell suppression is specific to nSMase2 inhibition (Figure 3b and Supplementary Fig. S3a). The inhibitor of nSMase2 did not affect T-cell proliferation when T-cells were treated in the absence of CAF-MDSCs (Supplementary Fig. S3b). Both compounds did not exhibit a reduction in the viability of CAF-MDSCs, indicating that the decreased suppressive activity is not due to compound toxicity (Supplementary Fig. S3c). The observed reduction in suppressive activity is likely attributed to the

significant decrease in the amount of EVs released from the cells, as indicated by measurements of total EV protein isolated from nSMase2i-treated CAF-MDSCs (Supplementary Fig. S3d). Next, EVs released by CAF-MDSCs, iDCs, M1 and M2 macrophages were isolated and purified by size exclusion chromatography and characterized by nanoparticle tracking analysis and flow cytometry (Supplementary Fig. S4).²³ Using this method specific for small EVs, the particles isolated from CAF-MDSC and iDC are between 108 and 120 nm in size; while EVs from M1 and M2 macrophage are between 75 and 97 nm in size (Figure 3c). The isolated EVs contain 80–93% of particles between 30 and 150 nm in size (Supplementary Fig. S4a) that display the surface markers CD63, CD9, and CD81 (Supplementary Fig. S4b). Negative markers of EVs proposed in MISEV 2018²³ include ApoA1/A2, ApoB and Alb. We quantified the levels of ApoB by LC-MS/MS and found an overall depletion of ApoB levels in EVs compared to levels in cells (Supplementary Fig. S4c), while ApoA1/A2 and Alb were not detected. Quantification of purified EVs showed that CAF-MDSCs produced significantly greater amounts of EVs than the other cell types while iDCs showed the least amount of EVs (Figure 3d). To determine whether EVs released by CAF-MDSCs directly inhibit T-cell proliferation, we treated autologous CD8+ T-cells with increasing amounts of CAF-MDSC EVs derived from coculture with 3 different CAF donors and found a concentration-dependent reduction in T-cell proliferation (Figure 3e). Next, we compared the suppressive effect of CAF-MDSC EVs with EVs derived from other myeloid cells by treating T-cells with equal amounts of EVs. We found that CAF-MDSC EVs significantly reduced the proliferation of T-cells of up to 25%, which is 2-fold greater in effect compared to iDC EVs at 12.5%, while M2 EVs showed a slight reduction of 7.5% and M1 EVs did not show any significant effect (Figure 3f).

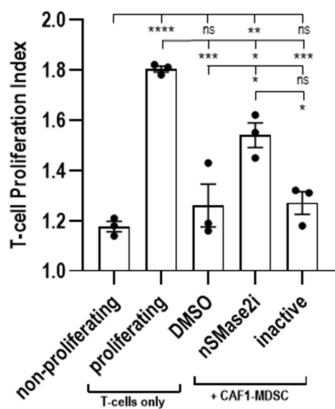
The protein cargo of CAF-MDSC EVs

To dissect how CAF-MDSC-derived EVs suppress T-cell proliferation, we profiled the protein cargo of EVs isolated from 3 independent donors of monocyte-derived cells (CAF-MDSC, iDC, M1, M2) using a Tandem Mass Tag (TMT)-based workflow (Figure 4a). A total of 196 proteins were identified in all samples (Supplementary Table S2). Taking the overlap of the CAF-MDSC proteome with the proteins in the corresponding EVs, 158 were shared while 38 proteins were found exclusively in the EVs (Figure 4b). Gene ontology enrichment of these 38 proteins showed that the majority of proteins consisted of extracellular matrix proteins. Out of the 196 total EV proteins, 190 are contained in Vesiclepedia (<http://microvesicles.org/>), a collection of experimentally validated EV proteins. Enrichment analysis of these proteins also showed gene ontology terms associated with EVs and the extracellular matrix (Figure 4c). We determined which proteins are enriched in CAF-MDSC EVs compared to other cell types and identified ten proteins that show significant enrichment in CAF-MDSC EVs. Functional protein network analysis in STRING¹⁵ (<https://string-db.org/>) revealed two association networks; one is composed of Laminin subunit beta-1 (LAMB1) and Laminin subunit gamma-1 (LAMC1) that

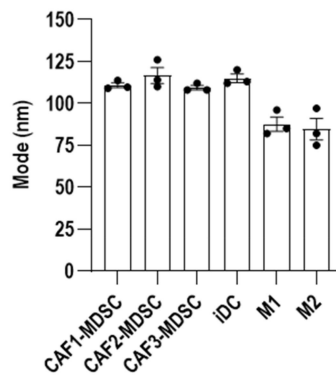
a) Investigating the role of EVs in T-cell suppression



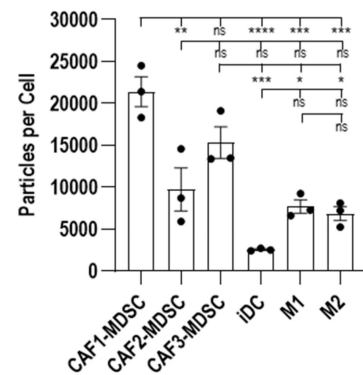
b) nSMase2 inhibition



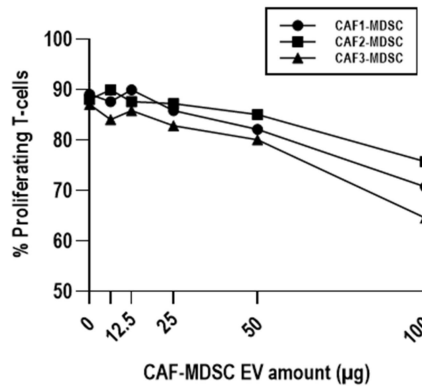
c) EV Size



d) EV Count



e) T-cell suppression by CAF-MDSC EVs



f) T-cell suppression by myeloid EVs

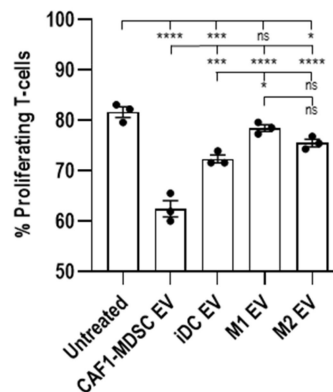


Figure 3. Suppression of autologous CD8 T-cell proliferation by CAF-MDSC extracellular vesicles (EV). Autologous CD8 T-cells were co-cultured with CAF-MDSC and treated with nSMase2 inhibitor (b) or treated with EVs (e-f) for 3 days then T-cell proliferation was measured by CFSE dilution using flow cytometry. (a) EVs released by CAF-MDSC can potentially suppress T-cell proliferation; this effect could be reversed by inhibiting the enzyme neutral sphingomyelinase 2 (nSMase2) that is important in EV generation. (b) Co-cultures of CAF-MDSCs and autologous CD8 T-cells were treated with an nSMase2 inhibitor (nSMase2i) or its inactive form. (c-d) EV characterization by nanoparticle tracking analysis to measure particle size and number. (e) Suppression of autologous CD8 T-cell proliferation by EVs released by CAF-MDSC using 6.25, 12.5, 25, 50, 100 µg EV or (f) 100 µg EVs isolated from myeloid cells based on protein content. Data shown is mean ± SEM from three independent experiments. Multiple group comparison by one-way ANOVA; ****= $p < 0.001$, ***= $p < 0.001$, **= $p < 0.01$, *= $p < 0.05$, ns = not significant.

form the laminin complex in the extracellular matrix and the second is composed of eight proteins – Osteopontin (SPP1), Metalloproteinase inhibitor 1 (TIMP1), Matrix metalloproteinase-9 (MMP9), Carbonic anhydrase 2 (CA2), Cytochrome c (CYCS), Triosephosphate isomerase (TPI1), Fructose-1,6-bisphosphatase 1 (FBP1) and Fructose-1,6-bisphosphatase 2 (FBP2) that are involved in the formation and regulation of the extracellular matrix, as well as

fructose metabolism²⁴ (Figure 4d). To interrogate the function of these proteins, we searched the chemogenomics database CHEMGENIE²⁵ for tool compounds. Three of the ten proteins (CA2, MMP9, and FBP1) have available tool compounds in the database. We selected one inhibitor for each protein based on the potency and selectivity that we then used in the T-cell functional assay. The CAF-MDSC/T-cell co-culture were treated with the

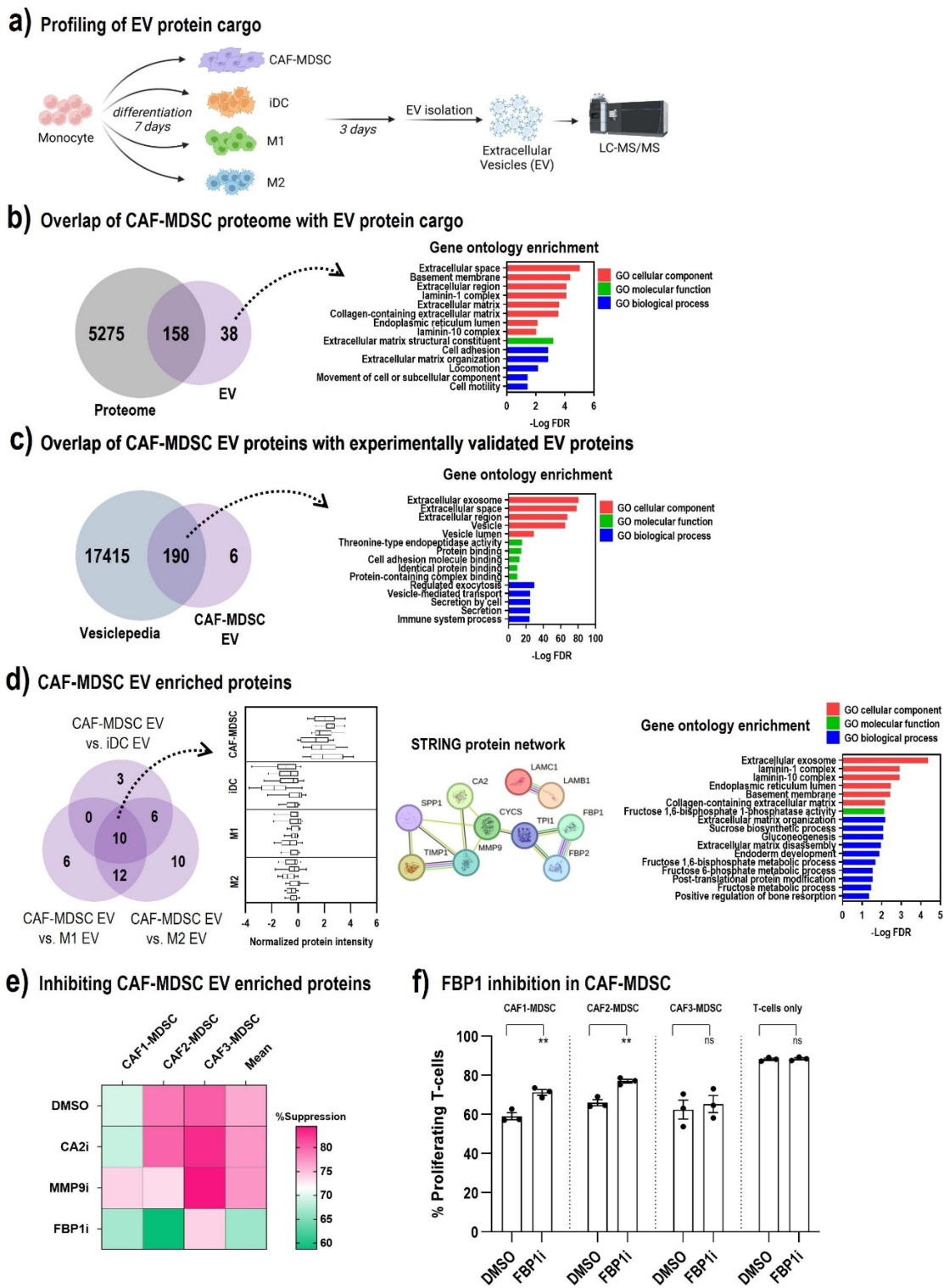


Figure 4. CAF-MDSC extracellular vesicle protein cargo. (a) Proteins contained in EVs isolated from monocyte-derived cells were quantified by TMT-based LC-MS/MS. (b) Overlap of CAF-MDSC EV proteins with CAF-MDSC proteome and gene ontology enrichment of proteins uniquely identified in the EV. (c) Overlap of CAF-MDSC EV proteins with experimentally validated EV proteins in the vesiclepedia database (<http://microvesicles.org/>) and gene ontology enrichment of CAF-MDSC EV proteins. (d) Venn diagram showing the overlap of significantly enriched proteins in CAF-MDSC EV vs. iDC EV or M1 EV or M2 EV; box plot of the normalized intensity of the 10 enriched proteins, each box represents one replicate in the LC-MS/MS analysis; functional protein network analysis and gene ontology enrichment of the 10 proteins using STRING DB. (e) CAF-MDSC/T-cell coculture were treated with inhibitors of CA2 (0.01 μ M), MMP9 (0.1 μ M), and FBP1 (10 μ M) then T-cell proliferation was measured by CFSE dilution assay. The percentage of suppression was calculated using the established formula: $((\text{Log}_2(y) \text{ of teff alone} - \text{Log}_2(y) \text{ of Teff+Myeloid cells}) / \text{Log}_2(y) \text{ of teff alone}) \times 100$, where y is the mean fluorescence intensity (MFI) of CFSE on the whole population divided by the MFI of CFSE of non-proliferating cells.¹⁶ (f) effect of FBP1 inhibition in CAF-MDSC on T-cell proliferation. Data shown is mean \pm SEM from three independent experiments. Multiple group comparison by one-way ANOVA; **= $p < 0.01$, * = $p < 0.05$, ns = not significant.

corresponding inhibitors CA2i, MMP9i, FBP1i, then T-cell proliferation was measured. Of the three inhibitors tested, FBP1i lowered the T-cell suppression of CAF-MDSC by 10% (mean of 3 donors), while CA2i and MMP9i did not affect CAF-MDSC activity (Figure 4e). Repeated experiments in the three donor-derived CAF-MDSCs showed a reversal of suppression as indicated by the significant increase in T-cell proliferation by FBP1 inhibition in CAF1-MDSC (12%) and CAF2-MDSC (11%), and a slight difference in CAF3-MDSC (3%) compared to the DMSO control while treatment of T-cells alone did not result in any change in cell proliferation (Figure 4f). Together, we pinpointed cargo proteins highly enriched in CAF-MDSC-derived EVs and show that among them, FBP1 can potentially curb T-cell proliferation and thus mediate the suppressive function of CAF-MDSCs.

Discussion

Extracellular vesicles, including exosomes, have been leveraged by tumor cells to modulate intercellular communication and evade T-cell surveillance in the TME. For example, tumors release PD-L1+ exosomes that bind to cytotoxic T-cells and impair their function, thus allowing tumors to avoid T-cell mediated killing.^{26,27,28} Additionally, the uptake of miR-92-containing CAF-derived exosomes can upregulate PD-L1 expression in breast cancer cells, further contributing to immune evasion.²⁹ Tumor-derived exosomes can also induce suppressive immune cells, such as MDSCs, *in vivo*.³⁰

Here, we showed that additional cell types other than tumor cells can help bypass T-cell surveillance by producing EVs. To dissect the modes of intercellular communication by which CAF-MDSC effect T-cell function, we first focused on measuring the cell surface proteome of CAF-MDSCs that include surface ligands and receptors that mediate cell-to-cell interactions. By quantifying changes in the cell surface proteomes among multiple myeloid cell subsets, we discovered that CAF-MDSCs have upregulated pathways and processes involving exocytosis and vesicle-mediated transport. This led us to hypothesize that CAF-MDSCs release EVs to curb T-cell activation. By inhibiting EV biogenesis controlled by nSMase2 in CAF-MDSCs, we demonstrated that these CAF-MDSCs have significantly reduced ability to suppress T-cell proliferation. Consistently, EVs isolated from CAF-MDSCs directly inhibit T-cell proliferation to a greater extent than EVs isolated from related myeloid cells. Of note, nSMase2 inhibition lead to increased secretion of microvesicles (MV) in a human breast cancer cell line³¹; additional studies are needed to define the role of CAF-MDSC derived MVs.

Given that cargo proteins are one of the key messengers in EVs to exert effects in target cells, pinpointing cargo proteins is critical for understanding EV function. However, there is very limited knowledge on protein cargo contents within EVs released by CAF-MDSCs or other myeloid cell subsets. To fill this gap, we have characterized the protein cargo of CAF-MDSC EVs and found that the enriched proteins are members and regulators of the extracellular matrix and fructose

metabolism. Using available tool compounds in the chemogenomics database,²⁵ we identified FBP1 as a possible mediator of T-cell suppression. FBP1 is a rate-limiting enzyme in gluconeogenesis, which plays a role in the dysfunction of natural killer cells by inhibiting glycolysis and viability.³² Further investigation may be warranted to understand whether the uptake of FBP1-containing EVs by T-cells cause aberrant glycolysis or if our observed reversal of T-cell suppression is due to the inhibition of FBP1 in EVs. Both tool compounds for CA2 and MMP9 did not affect the T-cell suppressive activity of CAF-MDSC in our assay. Reports indicate that both proteins may behave in a capacity that is not directed toward T-cell suppression. CA2 mediates carbon dioxide sensing by immune cells³³ while MMP9 acts to recruit myeloid cells in the TME.³⁴

Our study provides evidence supporting an EV-mediated mechanism of T-cell suppression by MDSCs induced by CAFs, which is independent of the direct influence of cancer cells. This finding aligns with our previous study, which demonstrated that inhibiting NOX2 function alone cannot fully reverse CD8+ T cell suppression. Hence, it suggests the presence of additional mechanisms involved in dampening CD8+ T cell proliferation. The current study explores an alternative mechanism, highlighting the role of CAF-MDSC-secreted EVs in suppressing T cell proliferation. A more detailed characterization of cargo contents in CAF-MDSC EVs, such as nucleic acids and lipids, and EV uptake by T-cells will elucidate this mechanism further. Given the emerging clinical studies have shown that the monocytic MDSC- and stromal-gene expression signatures are significantly correlated with poor response to anti-PD1 therapy for many tumor types, gaining new insights into the CAF-MDSC-T-cell axis in the context of stroma-rich tumors can provide prospective therapeutic avenues.² Further research is warranted to determine if our observations can be generalized across different types of MDSCs, thus enhancing the generalizability and broader understanding of MDSC-mediated immunosuppression. In addition, future investigations may explore the impact of MDSC-secreted EVs on CD4 T-cell responses and their potential implications in therapeutic resistance. Using this approach of unbiased proteome profiling of disease-relevant model systems, we can inform a screening strategy, such as the proof-of-concept small molecule screen in CAF-MDSCs in this study, to generate mechanistic hypotheses for targeting the CAF-MDSC axis, which can be extended to similar disease models and other tissue types.

Acknowledgments

This work was supported by the Merck & Co., Inc., Rahway, NJ, USA Research Laboratories Postdoctoral Research Program.

Disclosure statement

All authors are current or previous employees of Merck Sharp & Dohme LLC, a subsidiary of Merck & Co., Inc., Rahway, NJ, USA and shareholders of Merck & Co., Inc., Rahway, NJ, USA.

Funding

The author(s) reported there is no funding associated with the work featured in this article.

ORCID

Carlo P. Ramil  <http://orcid.org/0000-0002-1036-855X>

An Chi  <http://orcid.org/0000-0002-8213-1826>

Author contributions

C.P. Ramil and A. Chi conceptualized the study; C.P. Ramil, H. Xiang, J. Hai, and B. Ruprecht, designed the experiments, C.P. Ramil, H. Xiang, L. Cabral, P. Zhang, and A. Cronin performed the assays, co-culture, EV and proteomics experiments; C.P. Ramil, L. Cabral, and Z. Yin performed the EV characterization; C.P. Ramil, J. Hai, H. Xiang, D. Sun, Y. Jia, and H. Chen sourced and cultured cells from patient tissues; C.P. Ramil, H. Xiang and H. Wang identified and selected tool compounds for the assays; A. Chi supervised the study; C.P. Ramil wrote the manuscript with input from all authors.

References

- Vesely MD, Zhang T, Chen L. Resistance mechanisms to anti-PD cancer immunotherapy. *Annu Rev Immunol.* 2022;40(1):45–74. doi:10.1146/annurev-immunol-070621-030155.
- Cristescu R, Nebozhyn M, Zhang C, Albright A, Kobie J, Huang L, Zhao Q, Wang A, Ma H, Alexander Cao Z, et al. Transcriptomic determinants of response to pembrolizumab monotherapy across solid tumor types. *Clin Cancer Res.* 2022;28(8):1680–1689. doi:10.1158/1078-0432.CCR-21-3329.
- Singh L, Muise ES, Bhattacharya A, Grein J, Javaid S, Stivers P, Zhang J, Qu Y, Joyce-Shaikh B, Loboda A, et al. ILT3 (LILRB4) promotes the immunosuppressive function of tumor-educated human monocytic myeloid-derived suppressor cells. *Mol Cancer Res.* 2021;19(4):702–716. doi:10.1158/1541-7786.MCR-20-0622.
- Heim CE, Vidlak D, Kielian T. Interleukin-10 production by myeloid-derived suppressor cells contributes to bacterial persistence during staphylococcus aureus orthopedic biofilm infection. *J Leukoc Biol.* 2015;98(6):1003–1013. doi:10.1189/jlb.4VMA0315-125RR.
- Gillette MA, Satpathy S, Cao S, Dhanasekaran SM, Vasaiak SV, Krug K, Petralia F, Li Y, Liang W-W, Reva B, et al. Proteogenomic characterization reveals therapeutic vulnerabilities in lung adenocarcinoma. *Cell.* 2020;182:200–225.e35.
- Gato M, Blanco-Luquin I, Zudaire M, de Morentin XM, Perez-Valderrama E, Zabaleta A, Kochan G, Escors D, Fernandez-Irigoyen J, Santamaria E. Drafting the proteome landscape of myeloid-derived suppressor cells. *Proteomics.* 2016;16(2):367–378. doi:10.1002/pmic.201500229.
- Xiang H, Ramil CP, Hai J, Zhang C, Wang H, Watkins AA, Afshar R, Georgiev P, Sze MA, Song XS, et al. Cancer-associated fibroblasts promote immunosuppression by inducing ROS-generating monocytic MDSCs in lung squamous cell carcinoma. *Cancer Immunol Res.* 2020;8(4):436. doi:10.1158/2326-6066.CIR-19-0507.
- Hughes CS, Moggridge S, Müller T, Sorensen PH, Morin GB, Krijgsveld J. Single-pot, solid-phase-enhanced sample preparation for proteomics experiments. *Nat Protoc.* 2019;14(1):68–85. doi:10.1038/s41596-018-0082-x.
- Kulak NA, Pichler G, Paron I, Nagaraj N, Mann M. Minimal, encapsulated proteomic-sample processing applied to copy-number estimation in eukaryotic cells. *Nat Methods.* 2014;11(3):319–324. doi:10.1038/nmeth.2834.
- Ting L, Rad R, Gygi SP, Haas W. MS3 eliminates ratio distortion in isobaric multiplexed quantitative proteomics. *Nat Methods.* 2011;8(11):937–940. doi:10.1038/nmeth.1714.
- Cox J, Mann M. MaxQuant enables high peptide identification rates, individualized p.p.b.-range mass accuracies and proteome-wide protein quantification. *Nat Biotechnol.* 2008;26(12):1367–1372. doi:10.1038/nbt.1511.
- Tyanova S, Temu T, Sinitcyn P, Carlson A, Hein MY, Geiger T, Mann M, Cox J. The Perseus computational platform for comprehensive analysis of (prote)omics data. *Nat Methods.* 2016;13(9):731–740. doi:10.1038/nmeth.3901.
- Zecha J, Satpathy S, Kanashova T, Avanesian SC, Kane MH, Clauser KR, Mertins P, Carr SA, Kuster B. TMT labeling for the masses: a robust and cost-efficient, in-solution labeling approach. *Mol Cell Proteom.* 2019;18(7):1468–1478. doi:10.1074/mcp.TIR119.001385.
- Zhou Y, Zhou B, Pache L, Chang M, Khodabakhshi AH, Tanaseichuk O, Benner C, Chanda SK. Metascape provides a biologist-oriented resource for the analysis of systems-level datasets. *Nat Commun.* 2019;10(1):1523. doi:10.1038/s41467-019-09234-6.
- Szklarczyk D, Gable AL, Nastou KC, Lyon D, Kirsch R, Pyysalo S, Doncheva NT, Legeay M, Fang T, Bork P, et al. The STRING database in 2021: customizable protein–protein networks, and functional characterization of user-uploaded gene/measurement sets. *Nucleic Acids Res.* 2021;49(D1):D605–D612. doi:10.1093/nar/gkaa1074.
- Zaragoza B, Chen X, Oppenheim JJ, Baeyens A, Gregoire S, Chader D, Gorochov G, Miyara M, Salomon BL. Suppressive activity of human regulatory T cells is maintained in the presence of TNF. *Nat Med.* 2016;22(1):16–17. doi:10.1038/nm.4019.
- Bachurski D, Schuldner M, Nguyen P-H, Malz A, Reiners KS, Grenzi PC, Babatz F, Schauss AC, Hansen HP, Hallek M, et al. Extracellular vesicle measurements with nanoparticle tracking analysis – an accuracy and repeatability comparison between NanoSight NS300 and ZetaView. *J Extracell Vesicles.* 2019;8(1):1596016. doi:10.1080/20013078.2019.1596016.
- Morales-Kastresana A, Jones JC. Flow cytometric analysis of extracellular vesicles. In: Hill AF, editor *Exosomes and Microvesicles: methods and protocols*. New York, NY: Springer New York; 2017. pp. 215–225.
- Perez-Riverol Y, Bai J, Bandla C, Garcia-Seisdedos D, Hewapathirana S, Kamatchinathan S, Kundu DJ, Prakash A, Frericks-Zipper A, Eisenacher M, et al. The PRIDE database resources in 2022: a hub for mass spectrometry-based proteomics evidences. *Nucleic Acids Res.* 2022;50(D1):D543–D552. doi:10.1093/nar/gkab1038.
- Fagerberg L, Jonasson K, von Heijne G, Uhlén M, Berglund L. Prediction of the human membrane proteome. *PROTEOMICS.* 2010;10(6):1141–1149. doi:10.1002/pmic.200900258.
- Trajkovic K, Hsu C, Chiantia S, Rajendran L, Wenzel D, Wieland F, Schwille P, Brügger B, Simons M. Ceramide Triggers budding of exosome vesicles into multivesicular endosomes. *Sci.* 2008;319(5867):1244–1247. doi:10.1126/science.1153124.
- Rojas C, Barneva E, Thomas AG, Hu X, Southall N, Marugan J, Chaudhuri AD, Yoo S-W, Hin N, Stepanek O, et al. DPTIP, a newly identified potent brain penetrant neutral sphingomyelinase 2 inhibitor, regulates astrocyte-peripheral immune communication following brain inflammation. *Sci Rep.* 2018;8(1):17715. doi:10.1038/s41598-018-36144-2.
- Théry C, Witwer KW, Aikawa E, Alcaraz MJ, Anderson JD, Andriantsitohaina R, Antoniou A, Arab T, Archer F, Atkin-Smith GK, et al. Minimal information for studies of extracellular vesicles 2018 (MISEV2018): a position statement of the International Society for extracellular vesicles and update of the MISEV2014 guidelines. *J Extracell Vesicles.* 2018;7:1535750.
- Ellis R, Katerelos M, Choy SW, Cook N, Lee M, Paizis K, Pell G, Walker S, Power DA, Mount PF. Increased expression and phosphorylation of 6-phosphofructo-2-kinase/fructose-2,6-bisphosphatase isoforms in urinary exosomes in pre-eclampsia. *J Transl Med.* 2019;17(1):60. doi:10.1186/s12967-019-1806-6.
- Kutchukian PS, Chang C, Fox SJ, Cook E, Barnard R, Tellers D, Wang H, Pertusi D, Glick M, Sheridan RP, et al. CHEMGENTIE: integration of chemogenomics data for applications in chemical biology. *Drug Discov Today.* 2018;23(1):151–160. doi:10.1016/j.drudis.2017.09.004.

26. Poggio M, Hu T, Pai CC, Chu B, Belair CD, Chang A, Montabana E, Lang UE, Fu Q, Fong L, et al. Suppression of Exosomal PD-L1 Induces Systemic Anti-tumor Immunity and Memory. *Cell*. 2019;177(2):414–427.e13. doi:10.1016/j.cell.2019.02.016.
27. Chen G, Huang AC, Zhang W, Zhang G, Wu M, Xu W, Yu Z, Yang J, Wang B, Sun H, et al. Exosomal PD-L1 contributes to immunosuppression and is associated with anti-PD-1 response. *Nature*. 2018;560(7718):382–386. doi:10.1038/s41586-018-0392-8.
28. Yang Y, Li CW, Chan LC, Wei Y, Hsu JM, Xia W, Cha JH, Hou J, Hsu JL, Sun L, et al. Exosomal PD-L1 harbors active defense function to suppress T cell killing of breast cancer cells and promote tumor growth. *Cell Res*. 2018;28(8):862–864. doi:10.1038/s41422-018-0060-4.
29. Dou D, Ren X, Han M, Xu X, Ge X, Gu Y, Wang X. Cancer-associated fibroblasts-derived exosomes suppress immune cell function in breast cancer via the miR-92/PD-L1 pathway. *Front Immunol*. 2020;11:11. doi:10.3389/fimmu.2020.02026.
30. Xiang X, Poliakov A, Liu C, Liu Y, Deng Z-B, Wang J, Cheng Z, Shah SV, Wang G-J, Zhang L, et al. Induction of myeloid-derived suppressor cells by tumor exosomes. *Int J Cancer*. 2009;124(11):2621–2633. doi:10.1002/ijc.24249.
31. Menck K, Sönmezer C, Worst TS, Schulz M, Dihazi GH, Streit F, Erdmann G, Kling S, Boutros M, Binder C, et al. Neutral sphingomyelinases control extracellular vesicles budding from the plasma membrane. *J Extracell Vesicles*. 2017;6(1):1378056. doi:10.1080/20013078.2017.1378056.
32. Cong J, Wang X, Zheng X, Wang D, Fu B, Sun R, Tian Z, Wei H. Dysfunction of natural killer cells by FBP1-induced inhibition of glycolysis during lung cancer progression. *Cell Metab*. 2018;28(2):243–255.e5. doi:10.1016/j.cmet.2018.06.021.
33. Strowitzki MJ, Nelson R, Garcia MP, Tuffs C, Bleul MB, Fitzsimons S, Navas J, Uzielienė I, Ritter AS, Phelan D, et al. Carbon dioxide sensing by immune cells occurs through carbonic anhydrase 2-dependent changes in intracellular pH. *J Immunol*. 2022;208(10):2363–2375. doi:10.4049/jimmunol.2100665.
34. Melani C, Sangaletti S, Barazzetta FM, Werb Z, Colombo MP. Amino-Biphosphonate-Mediated MMP-9 inhibition breaks the tumor-bone marrow axis responsible for myeloid-derived suppressor cell expansion and macrophage infiltration in tumor stroma. *Cancer Res*. 2007;67(23):11438–11446. doi:10.1158/0008-5472.CAN-07-1882.